Nano Research

ISSN 1998-0124 CN 11-5974/O4
https://doi.org/10.1007/s12274-023-6309-3

Research Article

Highly adaptive and broadband triboelectric energy harvester with stretching silicone rubber strip for variable harmonic frequency vibration

Taili Du[1,2,§], Dianlong Shen[1,§], Ziyue Xi[1,§], Hongyong Yu[1] (✉), Fangyang Dong[1], Cong Zhao[1], Meixian Zhu[1], Yongjiu Zou[1,2] (✉), Peiting Sun[1,2], and Minyi Xu[1] (✉)

[1] *Dalian Key Laboratory of Marine Micro/Nano Energy and Self-powered Systems, Marine Engineering College, Dalian Maritime University, Dalian 116026, China*
[2] *Collaborative Innovation Research Institute of Autonomous Ship, Dalian Maritime University, Dalian 116026, China*
[§] *Taili Du, Dianlong Shen, and Ziyue Xi contributed equally to this work.*

Received: 11 September 2023 / **Revised:** 26 October 2023 / **Accepted:** 2 November 2023

ABSTRACT

An enormous number of wireless sensing nodes (WSNs) are of great significance for the Internet of Things (IoT). It is tremendously prospective to realize the *in-situ* power supply of WSNs by harvesting unutilized mechanical vibration energy. A harmonic silicone rubber triboelectric nanogenerator (HSR-TENG) is developed focusing on ubiquitous constant working frequency machinery. The unique design of the strip serving as a flexible resonator realizes both soft contact and high and broadband output. The significant factors influencing the 1st-order vibration mode of the strip are developed for realizing the harmonic frequency adaptation to external vibration. The surface treatment of the strip improves the output performance of HSR-TENG by 49.1% as well as eliminates the adhesion effect. The HSR-TENG is able to achieve a voltage output bandwidth of 19 Hz under a vibration strength of 3.0, showing its broadband capability. The peak power density of 153.9 W/m³ is achieved and 12 × 0.5 W light-emitting diodes (LEDs) are successfully illuminated by the HSR-TENG. It can continuously power a temperature sensor by harvesting the actual compressor vibration energy. In brief, the HSR-TENG provides a promising way for constant frequency vibration energy harvesting, so as to achieve *in-situ* power supply for the WSNs in the vicinity.

KEYWORDS

vibration energy harvesting, triboelectric nanogenerator, flexible silicone rubber strip, harmonic vibration, broadband

1 Introduction

The Internet of Things (IoT) technology has greatly contributed to the transformation of all the production and livelihood of human beings [1], including smart cities [2, 3], smart manufacturing, smart ocean [4, 5], smart transportations [6, 7], smart healthcare [8], etc. It is the foundation of the development of IoT to acquire massive data and working conditions mainly realized via numerous distributed wireless sensing nodes (WSNs) [9]. However, the power supply of these wireless sensing nodes has been facing with increasing challenges [10]. At present, most of the WSNs in the IoT system are mainly powered by batteries [11, 12]. However, traditional battery encounters various challenges [13–15], including limited life, high replacement and maintenance costs, and difficulties in replacing batteries within harsh environments or embedded in the structure. Additionally, environmental pollution caused by the after-treatment of the battery remains inadequately addressed due to its inherent properties [16]. According to a study by IDTechEx, at least 80% of the value of the IoT will be denied if batteries have to be replaced [17].

Meanwhile, during the operation of various mechanical devices utilized in our production and daily activities, a substantial amount of energy remains underutilized, including vibration [18, 19], acoustic [20], pressure [21], heat energy [22], etc. Among the various environmental energy sources, vibrations are generated by almost all machinery and equipment during their operation. While the energy produced by individual vibrations may be small, their input is stable and widespread. Consequently, vibrations are regarded as one of the most promising energy sources for powering WSNs in the era of IoT [23, 24]. In recent years, researchers have extensively studied the capture of vibrational energy using various methods, including electromagnetic [25], piezoelectric [26], and triboelectric mechanisms [27]. Among them, the triboelectric nanogenerator (TENG) was invented by Wang et al. in 2012 [28], and it is originated from Maxwell's Equation, and based on the combination of contact electrification and electrostatic induction [29]. Since it was invented, it has been widely applied to energy harvesting including wave energy [30–32], wind energy [33, 34], gas flow energy [35], human motion energy [36], etc., and self-powered sensing such as wave [37], tilt angle [38], wind speed [39], vortex [40], frequency [41] sensing, and so on. Especially, vibration energy harvesting based on triboelectric nanogenerator has garnered considerable attention

Address correspondence to Hongyong Yu, yuhongyong2020@dlmu.edu.cn; Yongjiu Zou, zouyj0421@dlmu.edu.cn; Minyi Xu, xuminyi@dlmu.edu.cn

due to its advantages [10, 42, 43], including great adaptability, high output, broad material selection, simple structure, low cost, and environmental friendliness.

Moreover, to ensure reliability and long service life of the mechanical equipment, as well as to ensure stability in delivering energy or serving the target objects, many mechanical devices are designed to operate at a relatively fixed frequency, which is always within the medium to low-frequency range. To efficiently harvest vibrational energy at a specific frequency, resonant structures employing cantilever or spring configuration are presented. Xu et al. proposed a spring-based TENG, which can achieve a peak power density of 240 mW/m^2 at a resonant frequency of 16 Hz [44]. A triple-cantilever based TENG designed by Yang et al. demonstrates a current of 55.7 μA and a power density of 252.3 mW/m^2 at the resonance frequency of 3.7 Hz [45]. While constant working frequency mechanical equipment generally maintains a stable frequency, it can still experience fluctuations within a certain range due to internal or external factors. Consequently, in the investigation of vibration energy harvesting from constant-frequency vibrations, it is imperative to encompass the energy harvesting characteristics within the range around the harmonic frequency point. To broaden the frequency band, Bhatia et al. presented a cascade impact structure TENG consisting of four layers spring-based TENG [46]. In addition, a vibration energy harvester (VEH) based on TENG developed by Qi et al. realizes high output within a broad range [47]. However, most of the VEH based on TENG adopts contact–separation mode [48], so relative motion between electrodes, which may affect the working of the machinery, is inevitable. Consequently, VEHs with springs or cantilevers based on freestanding TENG, in which there is no relative motion between electrodes and the vibrating machinery, are presented to solve this problem [10]. Even though, the presence of spring or cantilever structures poses significant challenges to the reliability of the VEH based on TENG. Moreover, the hard contact between the freestanding layer and the electrodes of the VEH based on freestanding TENG reduces its service life due to severe abrasion.

Therefore, a harmonic silicone rubber (HSR)-TENG working in freestanding mode is proposed for efficiently harvesting broadband vibration energy from constant working frequency machinery. The HSR-TENG adopts flexible silicone material with a high stretching rate and strong electronegativity as a resonant structure and freestanding layer, which has a simple structure and can realize soft contact and adjustable resonance frequency. Simultaneously, frequency band energy harvesting can be achieved by the non-linear stiffness variation due to the impact between silicone rubber and electrodes. The design of this work ensures that the electrical output of HSR-TENG not only reaches the maximum value at the harmonic frequency, but also maintains a usable range within the relevant frequencies around the harmonic frequency, which shows its broadband applicability. The maximum power density of the HSR-TENG achieves 349.45 W/m^3, and the bandwidth of it is up to 19 Hz with a vibration strength of 3.0. The experimental results reveal that HSR-TENG is capable of lighting up 12 × 0.5 W light-emitting diodes (LEDs) and continuously powering an aquarium thermometer. Finally, HSR-TENG is able to efficiently harvest the vibration energy of a marine air compressor for continuous power supply of a temperature sensor, exhibiting excellent application potential as a vibration energy harvester.

2 Results and discussion

2.1 Structure and working principle of the HSR-TENG

The application scenarios, structure, working principle, and the preparation process of the silicone rubber strip are shown in Fig. 1. As depicted in Fig. 1(a), many machinery and equipment are working under constant frequency, such as generator engines, air compressors, pumps, refrigerators, etc. The HSR-TENG possesses a great potential to collect the waste vibration energy produced during the operation of these devices to achieve the *in-situ* energy supply for the sensing nodes in their vicinity. Figure 1(b) illustrates the structure of the HSR-TENG, in which upper and lower frames are printed by the three-dimensional (3D) printer with polylactic acid (PLA), copper electrodes are adhered to two frames, and the silicone rubber strip is clamped at both ends of the frames to be fixed. The silicone rubber strip is one of the core elements in this work, and it is precisely due to its dynamic response to vibration excitation that it is capable of achieving contact and separation between the electrodes, thereby enabling the conversion of vibration energy into electric energy. Furthermore, silicone rubber is characterized by its strong electronegative properties and exhibits difference in the triboelectric series from copper, resulting in substantial charge transfer during contact and separation. The silicone rubber strip is fabricated by Ecoflex 00-30 part A and part B. The detailed fabrication process is shown in Fig. S1 in the Electronic Supplementary Material (ESM) and is described in detail in the Experimental section.

Aiming to analyze the characteristics of the strip, standard specimens of silicone strips of three different thicknesses were fabricated by means of a standard cutting tool, which is demonstrated in Fig. 1(c). It has been found that the maximum stretching rate exceeds 500% as a result of testing the standard specimens on a universal material testing machine. In accordance with the structural parameters of the HSR-TENG in this work, the modulus of elasticity of the strip ranging from 0%–100% stretching rate has been measured. As shown in Fig. 1(d), the modulus of elasticity is 0.045 MPa calculated with the mean value of different thicknesses strips, which provides the basis for further simulation analysis. With the benefit of well design and the properties of materials, as shown in Fig. 1(e), it is capable of restoring to its original state under different mechanical deformations such as stretching, bending, and twisting, exhibiting excellent flexibility and robustness.

The working principle of HSR-TENG is shown in Fig. 1(f). The silicone rubber strip will oscillate under external vibration excitation, which results in contact–separation between the strip and electrodes attached to the upper and lower frames. Even more, soft contact between the strip and the copper electrodes is achieved due to the specific characteristics of the silicone rubber. The silicone rubber strip serves as the moving part and electronegative triboelectric layer of the HSR-TENG. The copper acts as both the electropositive triboelectric layer and the electrode. According to the different working modes of TENG, HSR-TENG can be regarded as the freestanding layer mode.

In the initial stage, several contact–separation cycles between the strip and the electrode will lead to positive and negative charges on the surface of the copper and the strip, respectively, which is demonstrated in Fig. 1(f)(i). Following, as illustrated in Fig. 1(f)(ii), the strip oscillates downward excited by mechanical vibration, which will lead to an unbalanced potential difference between upper and lower electrodes. Thus, electrons flow from the lower electrode to the upper one, generating electric current from the upper electrode to the lower one through an external circuit. Furthermore, electric potential balance between the upper and lower electrodes achieves again when the strip is back to the middle position of the HSR-TENG with the oscillation of the strip upwards from the lower electrode, thus electrons' transfer is ceased, which is exhibited in Fig. 1(f)(iii). After that, the strip oscillates to the upper electrode successively and the new potential

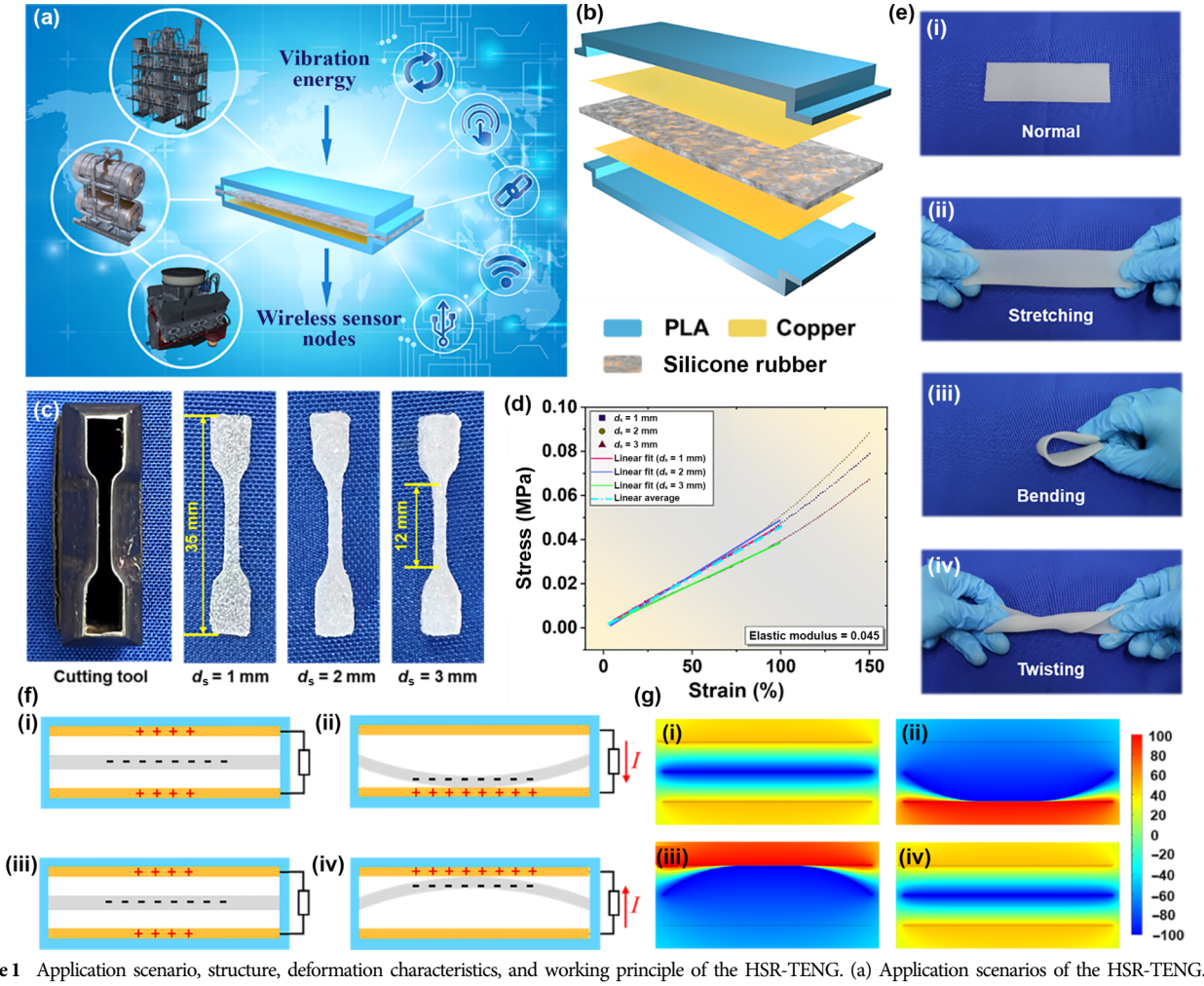

Figure 1 Application scenario, structure, deformation characteristics, and working principle of the HSR-TENG. (a) Application scenarios of the HSR-TENG. (b) Structure of HSR-TENG. (c) Standard cutting tool and specimens of silicone rubber strips of different thicknesses. (d) Modulus of elasticity of the silicone rubber strip. (e) Photographs of the HSR-TENG under (i) normal, (ii) stretching, (iii) bending, and (iv) twisting conditions. (f) Working principle of the HSR-TENG. (g) Potential distribution simulations of the HSR-TENG conducted by COMSOL.

unbalance results in an opposite electric current to that shown in Fig. 1(f)(ii) through the external circuit as represented in Fig. 1(f)(iv). Finally, the strip will oscillate to the middle position once again. The alternating current is generated by the cyclic oscillation of the strip under vibration excitation, thus converting the vibration energy into electric energy. Further, the working principle is also verified by the results of electrostatic field simulation conducted by COMSOL, which are indicated in Fig. 1(g). In addition, the HSR-TENG can also work in non-contact mode, which is presented in Fig. S2 in the ESM.

2.2 Kinematic characteristics of the silicone rubber strip

2.2.1 Theoretical analysis

According to the working principle of the freestanding layer triboelectric nanogenerator, the kinematic status of the strip subjected to vibration excitation has a significant influence on the output performance of the HSR-TENG. With the purpose of analyzing the kinematic characteristics of the strip, a coordinate system displayed in Figs. 2(a) and 2(b) is established, and the structural parameters employed in the kinematic analysis are exhibited in Figs. 2(a) and 2(b). The kinematic analysis of the strip can be classified into two processes considering its flexibility and the structure of the HSR-TENG. It is considered that the motion of the strip can be considered a linear deformation due to its own elasticity under vibration excitation when it oscillates with no upper and lower electrode constraints.

The kinetic characteristics of the strip would be analyzed by the Euler–Bernoulli beam theory [49, 50] and vibration of membrane theory [50]. This work conducts the analysis with sinusoidal vibration excitation, and its equation of motion can be expressed by Eq. (1)

$$z_v(x,t) = A_0 \sin\omega t \tag{1}$$

where $z_v(x,t)$ is the sinusoidal function of the vibration excitation, x means the direction perpendicular to the vibration direction, t is the time, A_0 is vibration amplitude, and ω is the angular frequency of the vibration, respectively. Therefore, the dynamic response of the flexible strip under vibration excitation is shown in Eq. (2) according to the Euler–Bernoulli beam theory

$$z(x,t) = A_0[\sin(\omega t) + \sum_{i=1}^{\infty} \frac{[\sin(\omega t) - (\omega/\omega_{ni})\sin(\omega_{ni} t)]}{\omega_{ni}^2[1-(\omega/\omega_{ni})^2]} f_{li}(x) \int_0^l f_{li}(x)\,\mathrm{d}x)] \tag{2}$$

where $z(x,t)$ is the dynamic response of the strip along the x direction, ω_{ni} is the i^{th} mode vibration frequency, $f_{li}(x)$ is the vibration mode function of the strip, and l is the length of the strip.

Furthermore, the dynamic response of the strip under vibration excitation is also characterized by membrane vibration in view of its width and flexibility. Thereby, the dynamic response of any point on the strip under vibration excitation can be determined by Eq. (3) in accordance with the membrane vibration theory

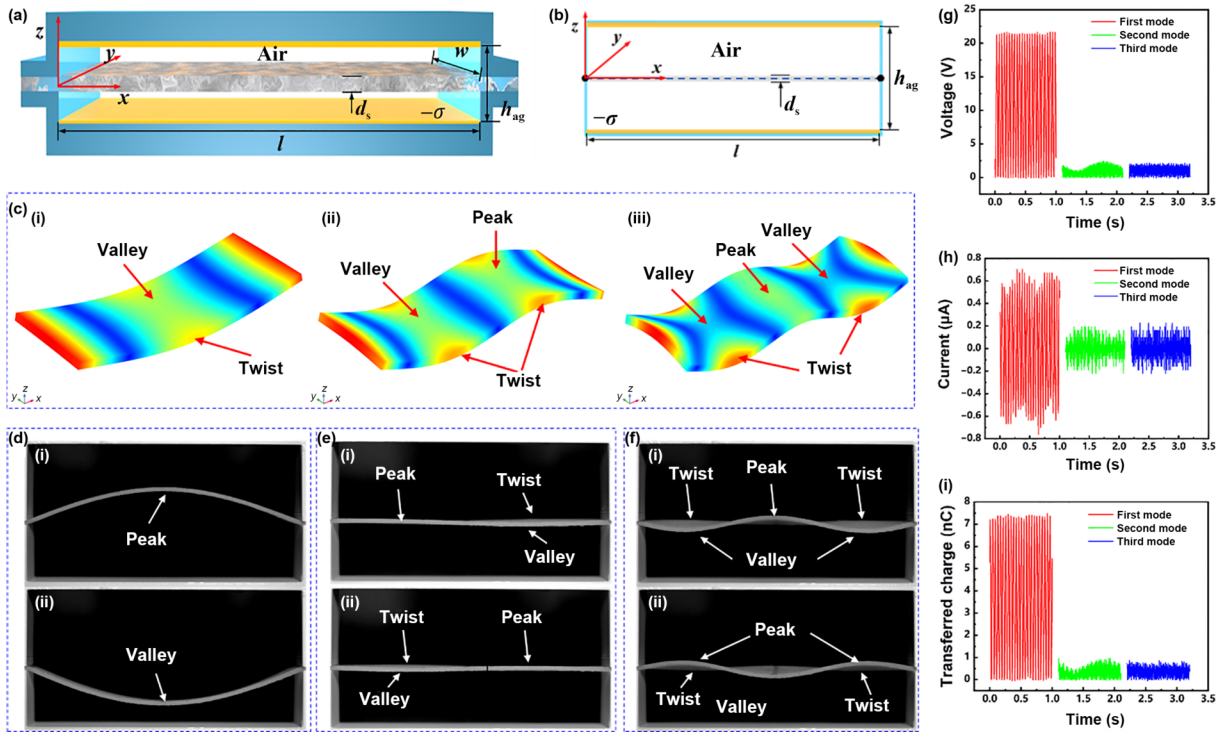

Figure 2 Kinematic characteristics of the silicone rubber strip. (a) 3D and (b) two-dimensional (2D) coordinate systems for analyzing the kinematic characteristics of the strip. (c) Simulation results of the (i) first-, (ii) second-, and (iii) third-order vibration modes of the silicone rubber strip. Kinematic responses captured by the high-speed camera under the (d) first-, (e) second-, and (f) third-order vibration modes of the silicone rubber strip. (g) Open-circuit voltage, (h) short-circuit current, and (i) transferred charge comparisons among different vibration modes.

$$z(x,y,t) = \left\{\frac{2}{\sqrt{\rho lw}}\sum_{m=1}^{\infty}\sum_{n=1}^{\infty}\sin\frac{m\pi x}{l}\cos\frac{n\pi y}{w}\left[\eta_{mn}(0)\cos\omega_{mn}t+\frac{\dot{\eta}_{mn}(0)}{\omega_{mn}}\sin\omega_{mn}t\right]\right\} + \left\{\frac{2}{\sqrt{\rho lw}}\sum_{m=1}^{\infty}\sum_{n=1}^{\infty}\frac{1}{\omega_{mn}}\sin\frac{m\pi x}{l}\cos\frac{n\pi y}{w}\int_0^t N_{mn}(\tau)\sin\omega_{mn}(t-\tau)\mathrm{d}\tau\right\} \quad (3)$$

In which, $z(x, y, t)$ is the dynamic response of the strip along the xy-plane, ρ is the density of the strip, w is the width of the strip, m and n mean different vibration modes, ω_{mn} is the natural frequencies of different orders, $\eta_{mn}(t)$ is the general coordinate, $N_{mn}(t)$ is got through mode decomposition method, and τ is the infinitesimal time. In addition, the linear deformation of the strip will be constrained as it collides with the upper and lower electrodes during oscillation, resulting in changes in its stiffness and damping coefficient, thus leading to the change from linear deformation to piecewise linear deformation [51, 52], which also means nonlinear deformation. Consequently, the dynamic response of the strip is governed by the combinational effects of the intrinsic property and dimensional parameters of the strip, the pretension force impact on the strip, the structural parameters of the frame, and the dynamic parameters of the vibration excitation. Even more, these factors will also contribute to the broadband output of the HSR-TENG.

2.2.2 *Vibration mode of the strip under vibration excitation*

To further investigate the vibration characteristics of the strip as well as its influence on the power generation characteristics of HSR-TENG, a simulation study of the strip vibration mode was conducted by employing the finite element analysis (FEA) method. Generally, vibration modes at 1st- to 3rd-order natural frequencies were analyzed, in accordance with the need for structural and vibration analysis. In the FEA analysis, the number of strip meshing is 16,000, after a comprehensive consideration of the analysis accuracy and the amount of computation, and the meshing diagram is shown in Fig. S3 in the ESM. Figures 2(c)(i)–2(c)(iii) illustrate the 1st- to 3rd-order vibration modes of the strip. It can be observed that there is only one peak (or valley) in the 1st-order vibration mode, one peak and one valley at the same time in the 2nd-order vibration mode, and two peaks (or valleys) and one valley (or peak) in the 3rd-order vibration mode. Meanwhile, it is found that there are twists at different parts of the strip in addition to the bending characteristics at different vibration modes. Therefore, a high-speed camera has been utilized to capture the kinetic images of the strip under different vibration modes to verify the simulation results mentioned above, which is demonstrated in Fig. 2(d). For the tests under different vibration modes, the vibration strength is maintained identically to 1.5, so that the vibration of the flexible strip will be analyzed more precisely. The vibration strength can be got by Eq. (4) as follows

$$\Gamma = a_{\max}/g = A_0\omega^2/g \quad (4)$$

where Γ is the vibration strength, which is the dimensionless shaking acceleration equaling to the ration of the maximum acceleration produced by vibration excitation, $a_{\max}$ is the maximum acceleration produced by vibration excitation to the gravitational acceleration, and g is the gravitational acceleration.

As depicted in Fig. 2(d), the strip primarily exhibits a bending state similar to a beam under the 1st-order vibration mode. However, the strip shows twists at the edge parts under the 2nd- and 3rd-order vibration modes in addition to bending deformations, which are depicted in Figs. 2(e) and 2(f). Moreover, the vibration amplitude at the 1st-order vibration mode is larger than that at the 2nd- and 3rd-order vibration modes, while the vibration frequency of the 1st-order mode is much lower than that at the 2nd and 3rd ones. According to the working principle of freestanding mode TENG, the output performance is positively proportional to the contact area and contact–separation frequency between the strip and the electrodes. Accordingly, the output

performance of the HSR-TENG has been tested under different vibration modes as displayed in Figs. 2(g)–2(i).

Figures 2(g)–2(i) illustrate the open-circuit voltage (V_{oc}), short-circuit current (I_{sc}), and transferred charge (Q_{sc}) with the strip under the 1st–3rd-order vibration modes, respectively. Thereby, it is obvious that the output performance of HSR-TENG with the strip under the 1st-order vibration mode is significantly superior to the output when the strip is at the 2nd- and 3rd-order vibration modes. The dynamic response captured by the high-speed camera is shown in Fig. S4 in the ESM. Although the high frequency under the higher-order vibration mode can accelerate the rate of charge transfer, there is counteracting effect due to the simultaneous existence of peaks and valleys in the strip when it is in the 2nd- and 3rd-order modes. In addition, since there is only one peak or valley under the 1st-order mode, and the amplitude of the strip is much larger than that under the higher-order mode, the output performance of HSR-TENG under the 1st-order mode of the strip has a significant advantage over that under the 2nd- and 3rd-order modes.

2.2.3 Analysis of the 1st-order mode vibration frequency of the strip

According to the above analysis of the key factors on the dynamic response characteristics of the strip and the output performance of HSR-TENG, the influences of the strip length, thickness, and pretension force on the 1st-order mode frequency (FOMF) of the strip were investigated. Figure 3(a) presents the experimental platform designed for FOMF testing of the strip. The strip was clamped by the specially designed support, which was fixed to the vibration exciter. On the upper part of the support, a displacement sensor was arranged to detect the central point vibration amplitude of the strip to decide the FOMF. The relative position of the displacement sensor to the support was fixed, eliminating the effect of exciter amplitude and enabling accurate monitoring of the amplitude of the strip under vibration excitation.

As shown in Fig. 3(b), the vibration amplitude of the strip with length (l) of 10 cm, thickness (d_s) of 1 mm, and stretching rate (s_t) of 20%, which are utilized to represent the pretension, shows that the FOMF is 22 Hz. The influences of strip length, thickness, and pretension on the FOMF are illustrated in Figs. 3(c)–3(e), respectively. The symbols in Figs. 3(c)–3(e), such as 10-2-20%, represent that the length of the strip is 10 cm, the thickness is 2 mm, and the stretching rate is 20%, while others are similar to that. Figure 3(c) reveals that the FOMF of the strip enlarges, while the amplitude decreases, along with the increase of the strip length. It is demonstrated in Fig. 3(d) that the strip thicknesses of 1, 2, and 3 mm have little impact on the FOMF and amplitude. In Fig. 3(e), the test results display that the FOMF of the strip raises as well as the strip is stretched further. The test results of other cases are depicted in Fig. S5 in the ESM. It should be noted that the thickness of the strip has little effect on its FOMF in cases that the lengths of the flexible tape are 10 and 15 cm, as shown in Fig. 3(d) and Fig. S5 in the ESM. However, the FOMF of the strip changes with the thickness with the strip length of 5 cm. This is mainly attributed to the torsional response when the length of the strip is short, which affects its FOMF.

An orthogonal trial considering the interactions among the factors, including length (l), thickness (d_s), and stretching rate (s_t), was designed to further determine the "significant" factors affecting the FOMF of the strip, and the results of the orthogonal trial are shown in Table S1 in the ESM. After analyzing the interactions between length and thickness, and between thickness and stretching rate, it is shown that the effect of them on the FOMF is "insignificant" after the Friedman verification. However, the Friedman value (F value) of the interaction between length and stretching rate is 6.684, which is larger than the Friedman value of 4.579 of $F_{0.01}$, showing a "highly significant" influence on the FOMF. Table 1 exhibits the significant analysis of factors that impact on FOMF of the strip. Therefore, the FOMF can be adjusted by changing the length, stretching or both of them adapting to external vibration frequency to achieve great output performance of the HSR-TENG, offering valuable guidance to enhance the scalability of HSR-TENG in harvesting vibration energy at different harmonic frequencies.

2.3 Output performance of the HSR-TENG

2.3.1 Output performance under different vibration amplitudes

As the external vibration frequency coincides with the FOMF of the strip, the vibration strength of the excitation source will then have an impact on the amplitude of the strip. Figures 4(a)–4(c)

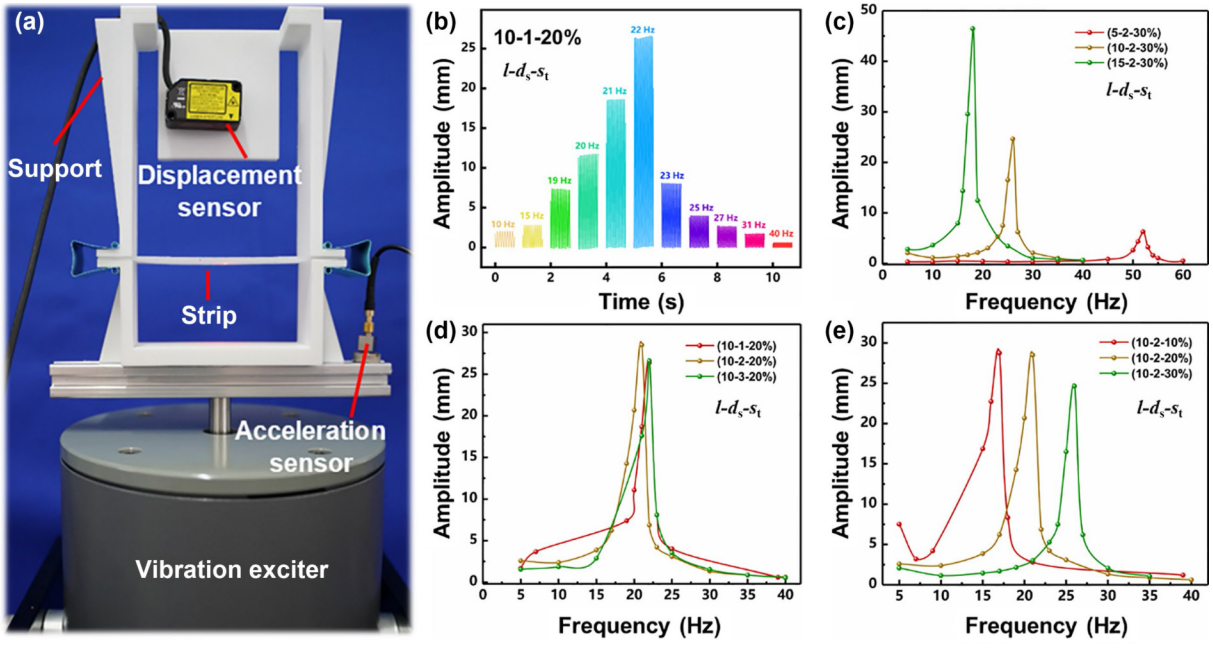

Figure 3 Analysis of the first-order mode vibration frequency of the strip. (a) Experimental platform designed for FOMF testing of the strip. (b) Vibration amplitudes of the strip under different frequencies with the l = 10 cm, d_s = 2 mm, and s_t = 20%. Comparisons of the vibration amplitudes of the strip with different (c) lengths, (d) thicknesses, and (e) stretching rates under different frequencies.

Table 1 Significance analysis of factors impact on FOMF of the silicone rubber strip

Factors	Square deviation	Freedom	Mean square	*F* value	Significance
l	2944.296	2	1472.148	145.265	Highly
d_s	40.519	2	20.259	1.999	Not
s_t	716.074	2	358.037	35.329	Highly
$l \times s_t$	301.037	4	75.259	7.426	Highly
Error	162.148	16	10.134	—	—
Sum	4164.074	26	—	—	—

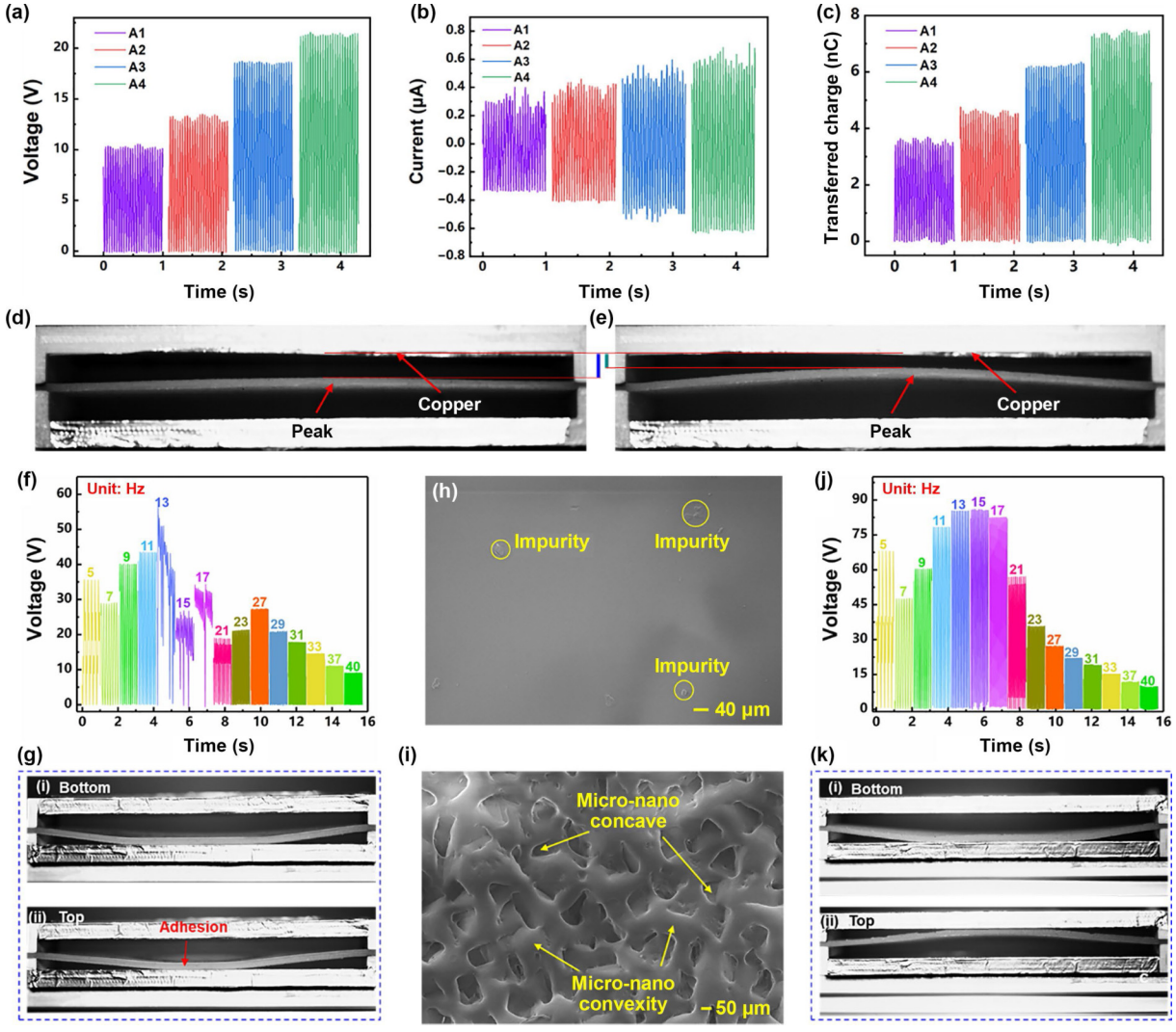

Figure 4 Output performance under different vibration amplitudes. (a) Open-circuit voltage, (b) short-circuit current, and (c) transferred charge under different vibration amplitudes. Kinematic responses under the vibration amplitudes of (d) A1 and (e) A4. (f) Open-circuit voltage of the HSR-TENG under different frequencies without the strip surface treatment. (g) Photos of strip adhesion to the electrode taken by high-speed camera. The SEM images of the strip surface (h) without and (i) with surface treatment. (j) Open-circuit voltage of the HSR-TENG under different frequencies with surface treatment of the strip. (k) Photos of strip separated well from the electrode taken by high-speed camera.

perform the V_{oc}, I_{sc}, and Q_{sc} of the HSR-TENG with different amplitudes under FOMF, respectively. The output performance improves along with the rise of the amplitude from A1 to A4 (A1–A4 represent different vibration amplitudes increasing gradually). The values of A1 to A4 are 0.432, 0.864, 1.296, and 1.727 mm, respectively. The V_{oc}, I_{sc}, and Q_{sc} are about 22 V, 0.6 μA, and 7.5 nC with an amplitude of A4, while they are only 10 V, 0.3 μA, and 3.6 nC with an amplitude of A1. Figures 4(d) and 4(e) show the kinematic images of the strip taken by a high-speed camera with the amplitudes of A1 and A4. It is observed that the acting distance and area between the strip and electrodes enlarge as the amplitude increases, which is also demonstrated in Fig. S6 in the ESM.

Noticeably, the above analysis is of the output performance when there is no contact between the strip and the electrode, which is linear deformation. Nevertheless, the strip will contact with or separate from the electrodes under the action of external vibration excitation. However, as displayed in Fig. 4(f), the output performance of the HSR-TENG becomes extremely unstable when the external vibration frequency is close to FOMF. As indicated in Fig. 4(g), the kinematic images show that the strip adheres to the electrode when they contact with each other, which affects the output of the HSR-TENG. This is because the untreated surface of the strip is too smooth, as reflected in the scanning electron microscopy (SEM) image in Fig. 4(h). When it contacts with the electrode, the air between them will be evacuated thus

forming a vacuum, which will influence the separation effect. Therefore, surface treatment is conducted, which is shown in Fig. 4(i), the micro-nano concave and convexity on the surface improve the contact and separation between the strip and electrode. So, the output performance is not only much more stable but also the V_{oc} of 85 V is about 49.1% higher than the V_{oc} of 57 V without surface treatment, which is displayed in Fig. 4(j). The primary reason for this change is attributed to micro-nano concave and convexity on the strip surface resulting from surface treatment, which significantly reduced the vacuum effect between the strip and the electrodes. This, in turn, leads to a more regular contact–separation between the strip and the electrodes of the HSR-TENG. The regular contact–separation, in particular, increased the effective contact area between the strip and the electrodes, resulting in a stable and enhanced output of the HSR-TENG. Moreover, the kinematic images illustrated in Fig. 4(k) indicate the well contact and separation during one vibration cycle. So, the strip with surface treatment will be employed to carry out the following study.

2.3.2 *Output performance under non-linear deformation of the strip*

It is clear from the above analysis that the length and stretching rate of the flexible strip have an influence on the FOMF to affect the output performance of HSR-TENG. However, although the effect of the strip thickness on the FOMF is not significant within the scope of this work, its contribution to the output performance of the HSR-TENG deserves to be further explored. Figure 5(a) and Fig. S7 in the ESM depict the output performance of the HSR-TENG with a length of 10 cm and thicknesses of 1–3 mm under the same stretching rate. As indicated in Fig. 5(a), the V_{oc} of the HSR-TENG with a strip thickness of 2 mm is 106 V, which is superior to 93.1 and 85.6 V of the HSR-TENGs with strip thicknesses of 1 and 3 mm, respectively. The I_{sc} and Q_{sc} comparisons among HSR-TENGs with different strip thicknesses are illustrated in Fig. S7 in the ESM. The reason for this is that, as displayed in Fig. 5(b)(i), the strip with a thickness of 1 mm is distorted under vibration excitation, thus affecting the charge transfer of the HSR-TENG. Meanwhile, although the strips with thicknesses of 2 and 3 mm perform no twisting as shown in Figs. 5(b)(ii) and 5(b)(iii), the contact area between the strip and electrode is smaller than that with a thickness of 2 mm due to the greater stiffness of the strip with a thickness of 3 mm. Therefore, the strip with a thickness of 2 mm will be adopted in the following.

In addition, the electrode spacing is another key factor, which is of significance to the output of HSR-TENG. In this work, HSR-TENGs with single side spacing (SP), which is represented by air gap between two electrodes (h_{ag})/2, of 4, 5, and 6 mm were introduced to be analyzed. It can be found in Fig. 5(c) that the V_{oc} of HSR-TENG with the SP of 5 mm is 134.1 V, which is higher than that with the SPs of 4 and 6 mm. The I_{sc} and Q_{sc} of the HSR-TENG with different SPs are demonstrated in Fig. S8 in the ESM, in which the I_{sc} and Q_{sc} of the HSR-TENG with SP of 5 mm also

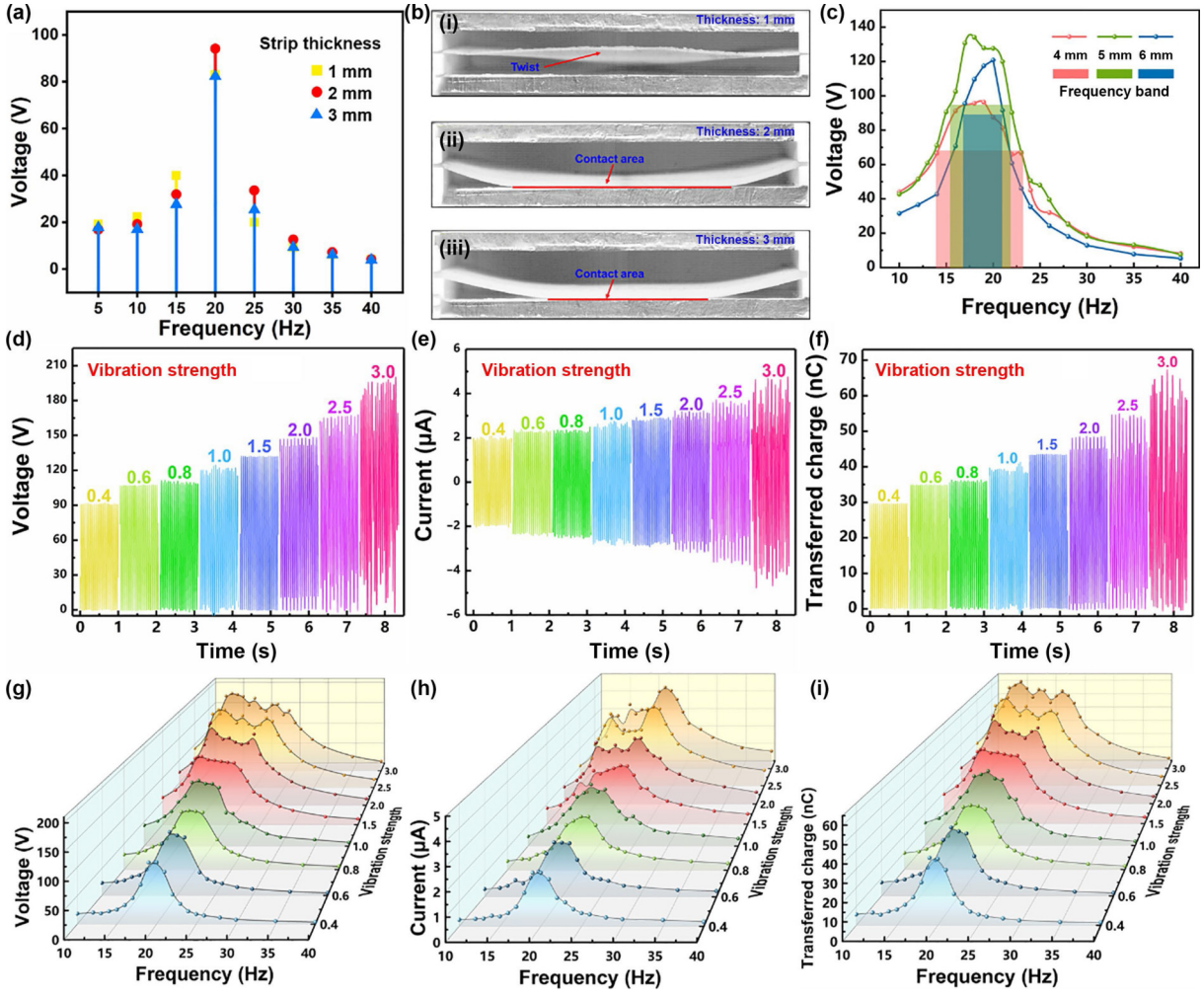

Figure 5 Output performance under non-linear deformation of the strip. (a) Open-circuit voltage of the HSR-TENG with a length of 10 cm and thicknesses of 1–3 mm. (b) Kinematic responses of the strip with thicknesses of (i) 1 mm, (ii) 2 mm, and (iii) 3 mm. (c) Open-circuit voltage and voltage bandwidth of the HSR-TENGs with different electrode spacings. (d) Open-circuit voltage, (e) short-circuit current, and (f) transferred charge under FOMF and different vibration strengths. (g) Open-circuit voltage, (h) short-circuit current, and (i) transferred charge under different vibration strengths.

got the highest value of 2.92 μA and 46.06 nC. Furthermore, the output bandwidth of the HSR-TENGs is impacted by the SP and exhibited in Fig. 5(c) and Fig. S8 in the ESM. The HSR-TENG with the SP of 4 mm has the largest bandwidth, but the output performance of it under the FOMF is the lowest. Thereby, the optimal structure with an SP of 5 mm is determined after comprehensive consideration of bandwidth and output at FOMF.

Furthermore, the vibration strength of external vibrations will vary with the load even under constant frequency conditions. Figures 5(d)–5(f) present the variation of V_{oc}, I_{sc}, and Q_{sc} as the HSR-TENG varies with vibration strength after it is adjusted to a specific FOMF, which is the same as the external vibration frequency. Thanks to its flexibility and harmonic resonance characteristics, the HSR-TENG is capable of generating output of 90 V, 2 μA, and 30 nC at a vibration strength of only 0.4. The V_{oc}, I_{sc}, and Q_{sc} of the HSR-TENG rise with increasing vibration strength in the range of 0.4–3.0, reaching ~ 180 V, 4 μA, and 60 nC at a vibration strength of 3.0. However, as shown in the figure, the output of HSR-TENG gradually becomes unstable when the vibration strength exceeds 2. When vibration strength is less than 1.5, there is uniform contact–separation between the strip and the electrode, so that the output signal is stable. On the other hand, when the vibration strength is greater than 2, the collision between the strip and the electrode is reinforced, thus the separation moments at different positions of the strip from the electrode are different under the effect of augmented collision force. Therefore, it will result in the instability of the output signal at higher vibration strength.

The broadband output characteristics of HSR-TENG under different vibration strengths are also demonstrated in Figs. 5(g)–5(i), in addition to effective constant-frequency energy harvesting. According to the piecewise linear model, the collision bandwidth between the strip and electrode will be broadened as the amplitude of the strip increases along with the increment of the vibration strength, which in turn causes the output bandwidth enhancement of the HSR-TENG. It is verified by the test results indicated in Figs. 5(g)–5(i). Additionally, the bandwidth of the V_{oc}, I_{sc}, and Q_{sc} is analyzed and illustrated in Fig. S9 in the ESM. In this work, the half power bandwidth, which refers to the frequency range where the electrical output of the HSR-TENG exceeds $1/\sqrt{2}$ (or 0.707) of the peak value at the harmonic frequency, is utilized to represent the usable range within the relevant frequencies around the harmonic frequency. Taking the half-power bandwidth of the HSR-TENG output-frequency response curve at a vibration strength of 0.4 as a reference, the bandwidth of V_{oc}, I_{sc}, and Q_{sc} broadens from 3 to 17–19 Hz as the vibration strength varies from 0.4 to 3.0. Although the output is not stable due to the large collision force at high vibration strength, the output performance and bandwidth of the HSR-TENG still improve, which shows its prospect in constant and broadband vibration energy harvesting.

2.4 Demonstration of the HSR-TENG

Based on the above analysis, the FOMF of 24 Hz, which is equal to the actual working frequency of a marine air compressor, was determined and adjusted to demonstrate the performance of the HSR-TENG. Firstly, the demonstration of HSR-TENG was carried out in the laboratory excited by the vibration exciter. As shown in Fig. 6(a), the output current of the HSR-TENG decreases with increasing the matching resistance. The power of 6.16 mW and the power density of 153.9 W/m³ are obtained with the matching resistance of 300 MΩ. Further, storing the electric energy harvested by the HSR-TENG in the capacitor to power the sensing node in the vicinity is an effective method to achieve *in-situ* power supply, so the capacitor charging characteristics of HSR-TENG were investigated, which is depicted in Fig. 6(b). Different capacitors of 47, 100, 220, 330, 470, and 1000 μF were charged to 12.24, 5.14, 3.51, 2.64, 2.10, and 0.69 V, respectively, in 300 s.

To verify its power capability, as displayed in Fig. 6(c) and Video ESM1, the HSR-TENG is able to power a commercial temperature sensor continuously. Even more, Fig. 6(d) and Video ESM2 demonstrate that 12 × 0.5 W LEDs are successfully illuminated when the HSR-TENG is under the vibration frequency of 24 Hz excited by the vibration exciter. At last, to demonstrate the prospective applications of the HSR-TENG in the constant-frequency vibration energy harvesting, the HSR-TENG

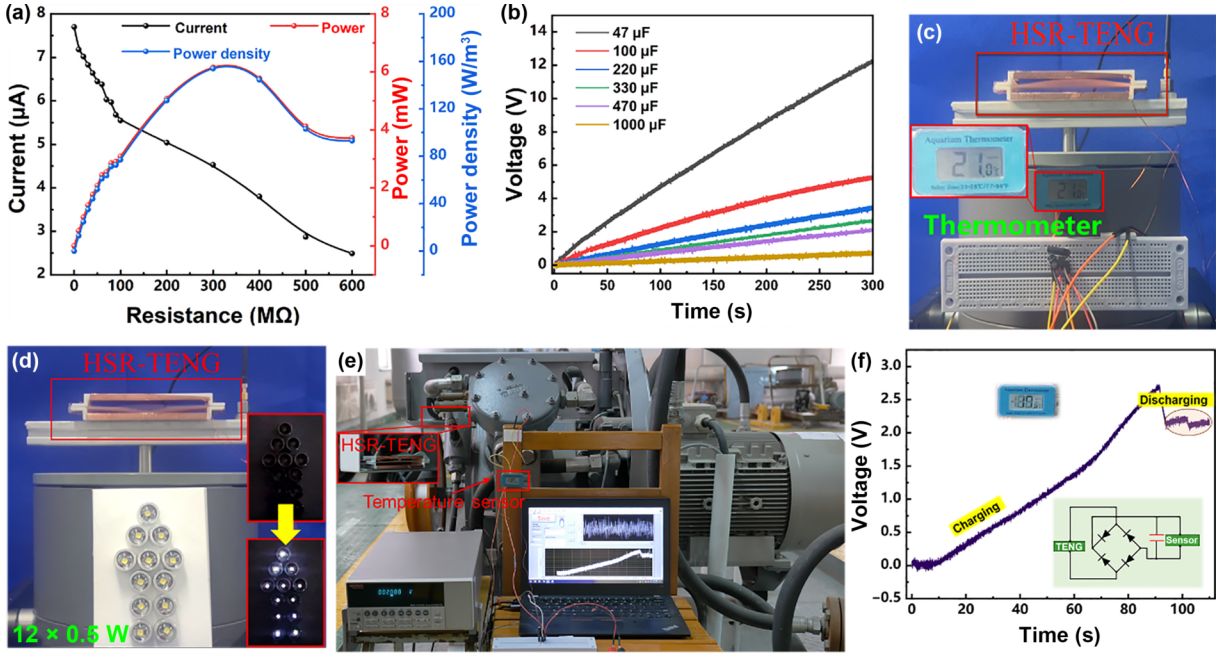

Figure 6 Demonstration of the HSR-TENG. (a) Output current, calculated power, and power density varying with matching resistance. (b) Different capacitors voltage curves charged by the HSR-TENG within 300 s. (c) A commercial temperature sensor is powered and (d) 12 × 0.5 W LEDs are lit up by the HSR-TENG arranged on the vibration exciter. (e) Continuous power supply for the temperature sensor by the HSR-TENG arranged on an actual air compressor. (f) Capacitor charging and discharging curve for continuous power supply for the temperature sensor.

was arranged on an actual marine air compressor to harvest the vibration energy during its working process. The model of the air compressor is XW090, and the main design and working parameters are illustrated in Table S2 in the ESM. The actual arrangement and experimental setup of the HSR-TENG on the air compressors are demonstrated in Fig. 6(e) and Fig. S10 in the ESM. The HSR-TENG was arranged on the platform between the first- and second-stage cylinder of the compressor and the environmental temperature during testing was about 17 °C in spring season. As illustrated in Fig. 6(e) and Video ESM3, the HSR-TENG is capable of powering the temperature sensor sustainably after charging the capacitor for 70 s. The charging and discharging curve of the capacitor for powering the temperature sensor is indicated in Fig. 6(f) and Video ESM3. It can be seen that the capacitor is charged to about 2.7 V firstly, and then the temperature sensor is switched on. During the discharging process, the voltage of the capacitor is lowered to about 2 V and keeps relative steady for about 29 s. The test results indicate that the discharging of the HSR-TENG has great potential to meet the continuous power requirements of the temperature sensor after being charged to about 2.7 V. In brief, the HSR-TENG has a promising prospect in harvesting constant frequency and broadband vibration energy, which provides a novel way to achieve *in-situ* power supply of the sensing nodes in the vicinity.

3 Conclusions

In summary, a harmonic silicone rubber triboelectric nanogenerator is proposed and systematically investigated for constant frequency and broadband mechanical vibration energy harvesting. The silicone rubber strip is introduced to act as both a freestanding layer and a flexible resonate structure, which has the potential to ensure long-term stability and durability of the HSR-TENG due to its specific inherent property and soft contact with the electrodes. The theoretical model of the strip considering bending and twisting is established to explore the working mechanism under forced harmonic vibration. Combining the kinematic response captured by a high-speed camera and electric output tested by the electrometer simultaneously, the output performance of the HSR-TENG under different vibration modes is discussed. The output under the 1st-order mode is several times that under the 2nd and 3rd modes. Then the significant factors, including strip length, stretching rate, and the interaction effect between them, impacting on the 1st-order mode frequency are analyzed according to the orthogonal test results. The surface treatment is presented to eliminate adhesion between the strip and electrode and improve the output performance by 49.1%. Based on the experimental findings, the HSR-TENG with a length of 10 cm, a strip thickness of 2 mm, and a single side spacing of 5 mm is determined to be the optimal device. The experimental results show that the output of HSR-TENG enhances along with the vibration strength, and is able to achieve a maximum output of 180 V, 4 μA, and 60 nC and voltage bandwidth of 19 Hz at a vibration strength of 3.0. The peak power density of 153.9 W/m^3 is achieved under a harmonic frequency of 24 Hz. Moreover, different capacitors are charged and 12 × 0.5 W LEDs are successfully lit up by the HSR-TENG, demonstrating its capability of vibration energy harvesting. Finally, a commercial temperature sensor is continuously powered by the HSR-TENG under the vibration of an actual air compressor. Therefore, the HSR-TENG has great prospects in mechanical vibration energy harvesting for the *in-situ* power supply of the WSNs in the era of IoT and intelligence. In future, we will further carry out research on encapsulation, material treatment, exquisite configuration, power management, large scale production technology, etc., for promoting the actual application of the HSR-TENG in the era of IoT.

4 Experimental section

4.1 Fabrication of the HSR-TENG

The HSR-TENG was mainly composed of frames, copper electrodes, and silicone rubber strip. The frame made of PLA was printed by the 3D printer with different lengths of 5, 10, and 15 cm, different SPs of 4, 5, and 6 mm, and a width of 4 cm. The copper electrodes were adhered to the upper and bottom frames. The main structure of the HSR-TENG was optimized from our previous work [53], which was redesigned with stretching strip rather than saggy one for adapting to broadband harmonic vibration. The fabrication process of the silicone rubber strip, which is the core component of the HSR-TENG, is shown in Fig. S1 in the ESM. The raw materials for fabricating the silicone rubber strip were Ecoflex 0030 part A and part B. Ecoflex 0030 part A and part B were poured into a container with a ratio of 1:1, and stirred homogeneously by agitating for tens of minutes. Then, the mixture was transferred to a deaeration container, in which vacuum was generated by a vacuum pump. The air in the mixture was eliminated because of the vacuum, thus enhancing the uniformity and even the strength of the product. Next, the defoamed mixture was poured into a well-designed mold, in which the sandpaper was attached to the upper and lower surfaces of the mold to conduct surface treatment. The designed mold was fabricated by the 3D printer to ensure the production of required strips with different lengths and thicknesses. Subsequently, the whole mold was put into a heating box to cure the mixture for 1 h at 50 °C. After that, the silicone rubber strip was peeled off from the mold, and the surface was cleaned with deionized water to remove the impurities. At last, the dried silicone rubber strip was affixed to the frame, completing the HSR-TENG fabrication process.

4.2 Analysis of the strip kinematic response

The kinematic response and output performance of the HSR-TENG were tested by the experimental setup shown in Fig. S11 in the ESM. The signal generator (UTG2062B) produced the vibration signal, and it was sent to drive the vibration exciter (JZK-50) after being amplified by a power generator (YE5874A). The kinematic response of the strip under vibration excitation was analyzed by the dynamic images taken by the high-speed camera (PHANTOM V2012), and the dynamic image was stored and treated in the phantom camera control (PCC) software interface together with the high-speed camera. The vibration amplitude of the strip was obtained by a displacement sensor (HG-C1050) together with a data acquisition system (DAQ280G) and a power processing module. The acceleration and vibration frequency of the HSR-TENG were measured by an acceleration sensor (KS 96.100) together with a signal processing unit (YND-1504).

4.3 Output performance measurement

As illustrated in Fig. S11 in the ESM, the output performance, including open-circuit voltage, short-circuit current, and transferred charge was measured by an electrometer (Keithley 6514), and then the electric signal was sent to the LabView-based computer for observation and storing through a data acquisition unit (NI-9215).

Acknowledgments

The work was supported by the National Natural Science Foundation of China (Nos. 52101345 and 52101400), the Scientific Research Fund of Liaoning Provincial Education Department (No. LJKZ0055), the Dalian Outstanding Young Scientific and Technological Talents Project (No. 2021RJ11), and the Open Fund of National Center for International Research of Subsea Engineering Technology and Equipment (No. 3132023354).

Electronic Supplementary Material: Supplementary material (fabrication process of the strip, experimental setup, kinematic response of the strip, output performance of the HSR-TENG, and detailed test results as shown in Figs. S1–S11, Tables S1 and S2, and demonstration Videos ESM1–ESM3) is available in the online version of this article at https://doi.org/10.1007/s12274-023-6309-3.

References

[1] Mori, H.; Kundaliya, J.; Naik, K.; Shah, M. IoT technologies in smart environment: Security issues and future enhancements. *Environ. Sci. Pollut. Res.* **2022**, *29*, 47969–47987.

[2] Liu, L.; Guo, X. G.; Lee, C. Promoting smart cities into the 5G era with multi-field Internet of Things (IoT) applications powered with advanced mechanical energy harvesters. *Nano Energy* **2021**, *88*, 106304.

[3] Abadía, J. J. P.; Walther, C.; Osman, A.; Smarsly, K. A systematic survey of Internet of Things frameworks for smart city applications. *Sust. Cities Soc.* **2022**, *83*, 103949.

[4] Deng, X. J.; Jiang, Y. L.; Yang, L. T.; Yi, L. Z.; Chen, J. Y.; Liu, Y.; Li, X. Y. Learning-automata-based confident information coverage barriers for smart ocean Internet of Things. *IEEE Internet Things J.* **2020**, *7*, 9919–9929.

[5] Qiu, T.; Zhao, Z.; Zhang, T.; Chen, C.; Chen, C. L. P. Underwater Internet of Things in smart ocean: System architecture and open issues. *IEEE Trans. Ind. Inform.* **2020**, *16*, 4297–4307.

[6] Aslam, S.; Michaelides, M. P.; Herodotou, H. Internet of ships: A survey on architectures, emerging applications, and challenges. *IEEE Internet Things J.* **2020**, *7*, 9714–9727.

[7] Zhu, F. H.; Lv, Y. S.; Chen, Y. Y.; Wang, X.; Xiong, G.; Wang, F. Y. Parallel transportation systems: Toward IoT-enabled smart urban traffic control and management. *IEEE Trans. Intell. Transp. Syst.* **2020**, *21*, 4063–4071.

[8] Chopade, S. S.; Gupta, H. P.; Dutta, T. Survey on sensors and smart devices for IoT enabled intelligent healthcare system. *Wirel. Pers. Commun.* **2023**, *131*, 1957–1995.

[9] Guiloufi, A. B.; El Khediri, S.; Nasri, N.; Kachouri, A. A comparative study of energy efficient algorithms for IoT applications based on WSNs. *Multimed. Tools Appl.* **2023**, *82*, 42239–42275.

[10] Du, T. L.; Dong, F. Y.; Xi, Z. Y.; Zhu, M. X.; Zou, Y. J.; Sun, P. T.; Xu, M. Y. Recent advances in mechanical vibration energy harvesters based on triboelectric nanogenerators. *Small* **2023**, *19*, 2300401.

[11] Dogra, R.; Rani, S.; Babbar, H.; Krah, D. Energy-efficient routing protocol for next-generation application in the Internet of Things and wireless sensor networks. *Wirel. Commun. Mob. Comput.* **2022**, *2022*, 8006751.

[12] Alaerjan, A. Towards sustainable distributed sensor networks: An approach for addressing power limitation issues in WSNs. *Sensors* **2023**, *23*, 975.

[13] Liazid, H.; Lehsaini, M.; Liazid, A. Data transmission reduction using prediction and aggregation techniques in IoT-based wireless sensor networks. *J. Netw. Comput. Appl.* **2023**, *211*, 103556.

[14] Singla, J.; Mahajan, R.; Bagai, D. An energy-efficient technique for mobile-wireless-sensor-network-based IoT. *ETRI J.* **2022**, *44*, 389–399.

[15] Jafari, M.; Khan, K.; Gauchia, L. Deterministic models of Li-ion battery aging: It is a matter of scale. *J. Energy Storage* **2018**, *20*, 67–77.

[16] Hayyat, M. U.; Nawaz, R.; Siddiq, Z.; Shakoor, M. B.; Mushtaq, M.; Ahmad, S. R.; Ali, S.; Hussain, A.; Irshad, M. A.; Alsahli, A. A. et al. Investigation of lithium application and effect of organic matter on soil health. *Sustainability* **2021**, *13*, 1705.

[17] Harrop, P. Battery elimination in electronics and electrical engineering 2018-2028. GlobeNewswire: United Kingdom, 2017.

[18] Chen, X. G.; Li, Y. M. Design, modeling, and testing of a vibration absorption device with energy harvesting based on force amplifier and piezoelectric stack. *Energy Conv. Manag.* **2022**, *255*, 115305.

[19] Yang, T.; Zhou, S. X.; Fang, S. T.; Qin, W. Y.; Inman, D. J. Nonlinear vibration energy harvesting and vibration suppression technologies: Designs, analysis, and applications. *Appl. Phys. Rev.* **2021**, *8*, 031317.

[20] Bansal, S.; Choi, C.; Hardwick, J.; Bagchi, B.; Tiwari, M. K.; Subramanian, S. Transmissive labyrinthine acoustic metamaterial-based holography for extraordinary energy harvesting. *Adv. Eng. Mater.* **2023**, *25*, 2201117.

[21] Xiao, H. F.; Pan, M.; Chu, J. Y. H.; Bowen, C. R.; Bader, S.; Aranda, J.; Zhu, M. L. Hydraulic pressure ripple energy harvesting: Structures, materials, and applications. *Adv. Energy Mater.* **2022**, *12*, 2103185.

[22] Chang, C.; He, X. Y.; Han, Z. Y.; Pei, L. L.; Wang, Z. Y.; Ji, Y. L. Harvesting thermal energy via tube-based triboelectric nanogenerators within an oscillating heat pipe. *Sustain. Energy Fuels* **2022**, *6*, 693–699.

[23] Roundy, S.; Wright, P. K.; Rabaey, J. A study of low level vibrations as a power source for wireless sensor nodes. *Comput. Commun.* **2003**, *26*, 1131–1144.

[24] Prajwal, K. T.; Manickavasagam, K.; Suresh, R. A review on vibration energy harvesting technologies: Analysis and technologies. *Eur. Phys. J. Spec. Top.* **2022**, *231*, 1359–1371.

[25] Basaran, S. Hybrid energy harvesting system under the electromagnetic induced vibrations with non-rigid ground connection. *Mech. Syst. Signal Proc.* **2022**, *163*, 108198.

[26] Zabek, D.; Pullins, R.; Pearson, M.; Grzebielec, A.; Skoczkowski, T. Piezoelectric-silicone structure for vibration energy harvesting: Experimental testing and modelling. *Smart Mater. Struct.* **2021**, *30*, 035002.

[27] Zhao, C. Y.; Yang, Y. W.; Upadrashta, D.; Zhao, L. Y. Design, modeling, and experimental validation of a low-frequency cantilever triboelectric energy harvester. *Energy* **2021**, *214*, 118885.

[28] Fan, F. R.; Tian, Z. Q.; Wang, Z. L. Flexible triboelectric generator. *Nano Energy* **2012**, *1*, 328–334.

[29] Guo, X.; Shao, J. J.; Willatzen, M.; Yang, Y.; Wang, Z. L. Theoretical model and optimal output of a cylindrical triboelectric nanogenerator. *Nano Energy* **2022**, *92*, 106762.

[30] Wang, Y.; Liu, X. Y.; Wang, Y. W.; Wang, H.; Wang, H.; Zhang, S. L.; Zhao, T. C.; Xu, M. Y.; Wang, Z. L. Flexible seaweed-like triboelectric nanogenerator as a wave energy harvester powering marine Internet of Things. *ACS Nano* **2021**, *15*, 15700–15709.

[31] Feng, J. R.; Zhou, H. L.; Cao, Z.; Zhang, E. Y.; Xu, S. X.; Li, W. T.; Yao, H. L.; Wan, L. Y.; Liu, G. L. 0.5 m triboelectric nanogenerator for efficient blue energy harvesting of all-sea areas. *Adv. Sci.* **2022**, *9*, 2204407.

[32] Ning, H.; Zhou, W. Y.; Tuo, L.; Liang, C. J.; Chen, C. J.; Li, S. Y.; Qu, H.; Wan, L. Y.; Liu, G. L. Tensegrity triboelectric nanogenerator for broadband blue energy harvesting in all-sea areas. *Nano Energy* **2023**, *117*, 108906.

[33] Tcho, I. W.; Kim, W. G.; Kim, J. K.; Kim, D. W.; Yun, S. Y.; Son, J. H.; Choi, Y. K. A flutter-driven triboelectric nanogenerator for harvesting energy of gentle breezes with a rear-fixed fluttering film. *Nano Energy* **2022**, *98*, 107197.

[34] Hu, X. Y.; Feng, J. R.; Liang, C. J.; Ning, H.; Chen, C. J.; Li, J. Y.; Wen, H. G.; Yao, H. L.; Wan, L. Y.; Liu, G. L. Round-trip oscillation triboelectric nanogenerator with high output response and low wear to harvest random wind energy. *Nano Res.* **2023**, *16*, 11259–11268.

[35] Taghavi, M.; Sadeghi, A.; Mazzolai, B.; Beccai, L.; Mattoli, V.

Triboelectric-based harvesting of gas flow energy and powerless sensing applications. *Appl. Surf. Sci.* **2014**, *323*, 82–87.

[36] Gao, Y. Y.; Xu, B. G.; Tan, D.; Li, M. Q.; Wang, Y. T.; Yang, Y. J. Asymmetric-elastic-structure fabric-based triboelectric nanogenerators for wearable energy harvesting and human motion sensing. *Chem. Eng. J.* **2023**, *466*, 143079.

[37] Shan, C. C.; He, W. C.; Wu, H. Y.; Fu, S. K.; Li, K. X.; Liu, A. P.; Du, Y.; Wang, J.; Mu, Q. J.; Liu, B. Y. et al. Dual mode TENG with self-voltage multiplying circuit for blue energy harvesting and water wave monitoring. *Adv. Funct. Mater.*, in press, DOI: 10.1002/adfm.202305768.

[38] Fang, L.; Zheng, Q. W.; Hou, W. C.; Gu, J. Y.; Zheng, L. A self-powered tilt angle sensor for tall buildings based on the coupling of multiple triboelectric nanogenerator units. *Sens. Actuators A: Phys.* **2023**, *349*, 114015.

[39] He, L. X.; Zhang, C. G.; Zhang, B. F.; Yang, O.; Yuan, W.; Zhou, L. L.; Zhao, Z. H.; Wu, Z. Y.; Wang, J.; Wang, Z. L. A dual-mode triboelectric nanogenerator for wind energy harvesting and self-powered wind speed monitoring. *ACS Nano* **2022**, *16*, 6244–6254.

[40] Wang, S. Y.; Xu, P.; Wang, X. Y.; Zheng, J. X.; Liu, X. Y.; Liu, J. H.; Chen, T. Y.; Wang, H.; Xie, G. M.; Tao, J. et al. Underwater bionic whisker sensor based on triboelectric nanogenerator for passive vortex perception. *Nano Energy* **2022**, *97*, 107210.

[41] Zhao, H. F.; Shu, M. R.; Ai, Z. H.; Lou, Z. R.; Sou, K. W.; Lu, C. Y.; Jin, Y. C.; Wang, Z. H.; Wang, J. Y.; Wu, C. S. et al. A highly sensitive triboelectric vibration sensor for machinery condition monitoring. *Adv. Energy Mater.* **2022**, *12*, 2201132.

[42] Zhang, X. H.; Zhao, J. Q.; Fu, X. P.; Lin, Y.; Qi, Y. C.; Zhou, H.; Zhang, C. Broadband vibration energy powered autonomous wireless frequency monitoring system based on triboelectric nanogenerators. *Nano Energy* **2022**, *98*, 107209.

[43] Bang, J.; Moon, I. K.; Jeon, Y. P.; Ki, B.; Oh, J. Fully wood-based green triboelectric nanogenerators. *Appl. Surf. Sci.* **2021**, *567*, 150806.

[44] Xu, M. Y.; Wang, P. H.; Wang, Y. C.; Zhang, S. L.; Wang, A. C.; Zhang, C. L.; Wang, Z. J.; Pan, X. X.; Wang, Z. L. A soft and robust spring based triboelectric nanogenerator for harvesting arbitrary directional vibration energy and self-powered vibration sensing. *Adv. Energy Mater.* **2018**, *8*, 1702432.

[45] Yang, W. Q.; Chen, J.; Zhu, G.; Wen, X. N.; Bai, P.; Su, Y. J.; Lin, Y.; Wang, Z. L. Harvesting vibration energy by a triple-cantilever based triboelectric nanogenerator. *Nano Res.* **2013**, *6*, 880–886.

[46] Bhatia, D.; Hwang, H. J.; Huynh, N. D.; Lee, S.; Lee, C.; Nam, Y.; Kim, J. G.; Choi, D. Continuous scavenging of broadband vibrations via omnipotent tandem triboelectric nanogenerators with cascade impact structure. *Sci. Rep.* **2019**, *9*, 8223.

[47] Qi, Y. C.; Liu, G. X.; Gao, Y. Y.; Bu, T. Z.; Zhang, X. H.; Xu, C. Q.; Lin, Y.; Zhang, C. Frequency band characteristics of a triboelectric nanogenerator and ultra-wide-band vibrational energy harvesting. *ACS Appl. Mater. Interfaces* **2021**, *13*, 26084–26092.

[48] Wardhana, E. M.; Mutsuda, H.; Tanaka, Y.; Nakashima, T.; Kanehira, T.; Taniguchi, N.; Maeda, S.; Yonezawa, T.; Yamauchi, M. Harvesting contact–separation-compression vibrations using a flexible and compressible triboelectric generator. *Sustain. Energy Technol. Assess.* **2020**, *42*, 100869.

[49] Scuciato, R. F.; Carrer, J. A. M.; Mansur, W. J. Dynamic analysis of Euler–Bernoulli beams by the time-dependent boundary element method formulation. *Eng. Anal. Bound. Elem.* **2016**, *63*, 134–153.

[50] Wang, C. Y.; Wang, C. M. *Structural Vibration: Exact Solutions for Strings, Membranes, Beams, and Plates*; CRC Press: Boca Raton, 2014.

[51] Narimani, A.; Golnaraghi, M. E.; Jazar, G. N. Frequency response of a piecewise linear vibration isolator. *J. Vib. Control* **2004**, *10*, 1775–1794.

[52] Qi, Y. C.; Liu, G. X.; Kuang, Y.; Wang, L.; Zeng, J. H.; Lin, Y.; Zhou, H.; Zhu, M. L.; Zhang, C. Frequency band broadening and charge density enhancement of a vibrational triboelectric nanogenerator with two stoppers. *Nano Energy* **2022**, *99*, 107427.

[53] Du, T. L.; Ge, B.; Mtui, A. E.; Zhao, C.; Dong, F. Y.; Zou, Y. J.; Wang, H.; Sun, P. T.; Xu, M. Y. A robust silicone rubber strip-based triboelectric nanogenerator for vibration energy harvesting and multi-functional self-powered sensing. *Nanomaterials* **2022**, *12*, 1248.